J. Fluid Mech. (2012), *vol.* 691, *pp.* 52–68.
doi:10.1017/jfm.2011.440

Axially homogeneous Rayleigh–Bénard convection in a cylindrical cell

Laura E. Schmidt[1], Enrico Calzavarini[2]†, Detlef Lohse[1], Federico Toschi[3,4] and Roberto Verzicco[1,5]

[1] Physics of Fluids, Department of Science and Technology, Impact and Mesa+ Institutes, and J. M. Burgers Center for Fluid Dynamics, University of Twente, PO Box 217, 7500 AE Enschede, The Netherlands

[2] Laboratoire de Mécanique de Lille, CNRS/UMR 8107, Université Lille 1, and Polytech'Lille, Cité Scientifique, Avenue P. Langevin, 59650 Villeneuve d'Ascq, France

[3] Department of Physics, and Department of Mathematics and Computer Science, and J. M. Burgers Center for Fluid Dynamics, Eindhoven University of Technology, 5600 MB Eindhoven, The Netherlands

[4] CNR-IAC, Via dei Taurini 19, 00185 Rome, Italy

[5] Department of Mechanical Engineering, University of Rome 'Tor Vergata', Via del Politecnico 1, 00133 Rome, Italy

(Received 5 April 2011; revised 8 September 2011; accepted 30 September 2011; first published online 1 December 2011)

Previous numerical studies have shown that the 'ultimate regime of thermal convection' can be attained in a Rayleigh–Bénard cell when the kinetic and thermal boundary layers are eliminated by replacing both lateral and horizontal walls with periodic boundary conditions (homogeneous Rayleigh–Bénard convection). Then, the heat transfer scales like $Nu \sim Ra^{1/2}$ and turbulence intensity as $Re \sim Ra^{1/2}$, where the Rayleigh number Ra indicates the strength of the driving force (for fixed values of Pr, which is the ratio between kinematic viscosity and thermal diffusivity). However, experiments never operate in unbounded domains and it is important to understand how *confinement* might alter the approach to this ultimate regime. Here we consider homogeneous Rayleigh–Bénard convection in a laterally confined geometry – a small-aspect-ratio vertical cylindrical cell – and show evidence of the ultimate regime as Ra is increased: in spite of the lateral confinement and the resulting kinetic boundary layers, we still find $Nu \sim Re \sim Ra^{1/2}$ at $Pr = 1$. Further, it is shown that the system supports solutions composed of modes of exponentially growing vertical velocity and temperature fields, with Ra as the critical parameter determining the properties of these modes. Counter-intuitively, in the low-Ra regime, or for very narrow cylinders, the numerical simulations are susceptible to these solutions, which can dominate the dynamics and lead to very high and unsteady heat transfer. As Ra is increased, interaction between modes stabilizes the system, evidenced by the increasing homogeneity and reduced fluctuations in the root-mean-square velocity and temperature fields. We also test that physical results become independent of the periodicity length of the cylinder, a purely numerical parameter, as the aspect ratio is increased.

Key words: buoyancy-driven instability, turbulent convection

† Email address for correspondence: enrico.calzavarini@polytech-lille.fr

1. Introduction

There has been longstanding scientific interest in the heat transfer in Rayleigh–Bénard convection (RBC) – when a fluid confined between two plates undergoes thermal convection due to a temperature difference between the cold top and hotter bottom plate (Siggia 1994; Kadanoff 2001; Ahlers, Grossmann & Lohse 2009; Lohse & Xia 2010). The dynamics of the system depends on the strength of the driving temperature difference (given by the Rayleigh number, Ra) and the ratio of the kinematic viscosity to the thermal diffusivity (given by the Prandtl number, Pr). Recently, studies of unconfined thermal convection – starting with the numerical work by Lohse & Toschi (2003) – were prompted by the relevance to natural convection phenomena, as occurs in the Earth's atmosphere (Celani *et al.* 2007) or in the core of stars (Garaud *et al.* 2010; Simitev & Busse 2010), and as a way to test theoretical predictions for the scaling of the heat transfer (given by the Nusselt number, Nu) and turbulence intensity (given by the Reynolds number, Re).

In the limit of high Ra it was proposed that the dynamics would reach an ultimate regime of thermal convection, which is dominated by the bulk flow rather than the viscous and thermal boundary layers (Kraichnan 1962). Within the Grossmann–Lohse theory of thermal convection, this regime where the dynamics does not depend on thermal plumes is also predicted (Grossmann & Lohse 2000, 2001, 2002). Under these conditions, the Reynolds and Nusselt numbers are predicted to scale like $Re \sim Ra^{1/2}$ and $Nu \sim Ra^{1/2}$, with different Pr scaling depending on the theory (Kraichnan 1962; Spiegel 1971; Grossmann & Lohse 2000, 2001, 2002). The question of the existence of this regime was addressed in simulations of homogeneous Rayleigh–Bénard convection in a tri-periodic cell (i.e. *without confinement*), where evidence was found supporting such a regime when all of the boundaries (and thus boundary layers) were absent (Lohse & Toschi 2003) and confirming (Calzavarini *et al.* 2005) the Prandtl number dependence, $Nu \sim Ra^{1/2}Pr^{1/2}$ and $Re \sim Ra^{1/2}Pr^{-1/2}$, as suggested by Grossmann & Lohse (2000, 2001, 2002). The statistical properties of the turbulent flow realized in such a system at high Ra numbers, with particular attention paid to its anisotropic fluctuations, were addressed in Biferale *et al.* (2003). Exponentially growing solutions at low Ra were analytically derived by Calzavarini *et al.* (2006) and observed in the simulations, appearing as 'elevator modes' composed of strong upward and downward jets, and coinciding with an increasing heat transfer until the modes became unstable and disintegrated. The instability thresholds and growing rates of the 'elevator mode' solutions turn out to be identical to those derived by Batchelor & Nitsche (1991) for the stability of a stratified fluid in an unbounded domain.

Later, experiments performed in long rectangular channels by Gibert *et al.* (2006, 2009) and Tisserand *et al.* (2010) and in cylindrical pipes by Arakeri *et al.* (2000) and Cholemari & Arakeri (2009) also found scaling laws consistent with those expected for the ultimate regime, despite the presence of the sidewalls, which cause an additional anisotropy and drag in the flow. They also observed a mean global flow composed of hot upward- and cool downward-moving columns. Whereas in standard RBC strong thermal gradients occur at the top and bottom plates, leaving the temperature field within the bulk flow nearly uniform, in the experiments with long cells, there exists a mean, linear temperature gradient throughout the bulk. It is this underlying linear gradient that is used to drive the convection in homogeneous RBC, and in the axially periodic convection cell considered here.

Instability of a stationary uniformly stratified fluid contained in a vertical circular cylinder was possibly first investigated by Halesa (1937), who was interested in the mechanism of geysers. Later on, Taylor (1954) investigated the same problem,

estimated the critical Rayleigh number for the appearance of convection and validated this result by means of experimental observations. Jones & Moore (1979) have studied the case of stress-free conditions at the cylinder wall. Finally Batchelor & Nitsche (1993) have taken into consideration the case in which the imposed initial stratification function, $\bar{T}(z)$, also has a sinusoidal profile. We address the interested reader to this latter work for a more detailed description of past analytical studies on this problem.

In the present work, we numerically and analytically investigate thermal convection in a long vertical cylinder, in both the low-Ra and high-Ra limits. Though the top and bottom boundary layers are absent, the sidewalls are still present as in the experimental situations. The objective is to find out whether also in this confined (and presumably more stabilizing) geometry exponentially growing solutions (so-called elevator modes) exist, how the Nusselt and Reynolds number depend on Ra, and how the results compare to recent experiments in confined flow geometries (Arakeri *et al.* 2000; Perrier, Morat & LeMouel 2002; Gibert *et al.* 2006, 2009; Cholemari & Arakeri 2009). We first derive exponentially growing mode solutions of the governing Boussinesq equations with laterally confined boundary conditions, and compare them with results from simulations. Then we increase Ra and find that interaction between the modes stabilizes the system. This interaction prevents the growth of the exponential modes, and allows us to define the global heat transfer and the global Reynolds number of the system.

2. The axially homogeneous Rayleigh–Bénard system and a class of analytic solutions

2.1. *Definition of the system*

The system under study is axially homogeneous thermal convection in a vertical cylinder, i.e. in a domain with periodic boundary conditions in the axial direction, but with lateral confinement. Standard Rayleigh–Bénard convection occurs in a cylinder (or other geometry) with top and bottom plates kept at fixed temperatures, and this temperature difference drives the flow. In the homogeneous or periodic case, with no boundaries except the radial wall, we drive the flow using a temperature gradient $\Delta' = \mathrm{d}\bar{T}/\mathrm{d}z$, where $\bar{T}$ is an underlying mean temperature profile (here assumed to be linear in z) about which the Θ fluctuations occur in experiments (Gibert *et al.* 2006, 2009). The diameter of the cylinder d is the only imposed scale, and therefore we make the hypothesis that d is the relevant length scale for the convection (aside from the additional smaller scales as turbulence develops). The periodicity length L, which can be combined with the diameter to form the aspect ratio $\Gamma = d/L$, is much less relevant because it does not change the forcing of the system. We non-dimensionalize the governing Navier–Stokes equations under the Boussinesq approximation using $\hat{x} = d$ for lengths, the free-fall speed $\hat{u} = \sqrt{\alpha g \Delta' d^2}$ for velocities, and $\hat{T} = \Delta' d$ for temperatures. The Prandtl number is $Pr = \nu/\kappa$ and the Rayleigh number is

$$Ra = \frac{\alpha g \Delta' d^4}{\nu \kappa}. \tag{2.1}$$

Here the material parameters are the coefficient of thermal expansion α, the kinematic viscosity ν, and the thermal diffusivity κ; the gravitational acceleration is denoted as g. Notice that the same definition of the Rayleigh number was chosen in the experimental studies by Gibert *et al.* (2006, 2009) and Tisserand *et al.* (2010). The more usual Rayleigh number based on the height of a closed Rayleigh–Bénard

cell, $Ra_L = \alpha g \Delta T L^3 (\nu\kappa)^{-1}$, where ΔT is the temperature difference between the horizontal plates, is linked to the present one through the relation $Ra_L = Ra\,\Gamma^4$.

In non-dimensional form, the Boussinesq equations read

$$\frac{\mathrm{D}\bar{u}}{\mathrm{D}t} = -\bar{\nabla} P + \sqrt{\frac{Pr}{Ra}}\nabla^2 \bar{u} + \Theta\,\hat{z}, \tag{2.2}$$

$$\frac{\mathrm{D}\Theta}{\mathrm{D}t} = \frac{1}{\sqrt{Pr\,Ra}}\nabla^2\Theta + w, \tag{2.3}$$

where $\bar{u} = (u, v, w)$ is the velocity field with components in the r, θ and z directions, respectively, P is the dimensionless pressure field, and the $\mathrm{D}/\mathrm{D}t$ symbol stands for the material derivative operator.

The velocity field satisfies the no-slip condition at the lateral walls located (in non-dimensional units) at $r = r_{ext} = 1/2$, so that

$$\bar{u}|_{r=1/2} = 0. \tag{2.4}$$

For the temperature T, we consider either a fixed condition at the lateral wall, which in terms of the fluctuations Θ means

$$\Theta|_{r=1/2} = 0, \tag{2.5}$$

or adiabatic conditions at the wall, corresponding to

$$\partial\Theta/\partial r|_{r=1/2} = 0. \tag{2.6}$$

The system defined so far models the physical situation of a vertical pipe connected to two infinite reservoirs of fluids at different temperatures. However, in real experiments, homogeneous convective systems are produced by connecting a vertical conduit to two closed and finite chambers filled with fluid at different temperatures (see e.g. Gibert *et al.* 2006; Cholemari & Arakeri 2009). Therefore, in order to mimic such a system in the following, it will be important to take into account the condition of no net vertical mass flux, which corresponds here to a zero total vertical momentum over any horizontal section (at any height z) in the system:

$$\int_0^{r_{ext}} \int_0^{2\pi} w r\,\mathrm{d}r\,\mathrm{d}\theta = 0. \tag{2.7}$$

Note that the definition of Θ already implies the condition $\int_0^{r_{ext}} \int_0^{2\pi} \Theta r\,\mathrm{d}r\,\mathrm{d}\theta = 0$ at any height z. The no net mass flux condition, however, does not prevent a bottom-up convective heat flow. We indeed expect $\int_0^{r_{ext}} \int_0^{2\pi} w\Theta r\,\mathrm{d}r\,\mathrm{d}\theta > C$, where C is positive, independent of z, but it can be time-dependent.

2.2. *Elevator mode solutions to governing equations*

As in the tri-periodic case, we look for solutions that are translationally invariant in z and have $u = v = 0$ (Calzavarini *et al.* 2006). The coupled equations for the vertical velocity $w(r, \theta, t)$ and temperature $\Theta(r, \theta, t)$ are then

$$\frac{\partial w}{\partial t} = \sqrt{\frac{Pr}{Ra}}\nabla^2 w + \Theta, \tag{2.8}$$

$$\frac{\partial \Theta}{\partial t} = \frac{1}{\sqrt{Pr\,Ra}}\nabla^2\Theta + w. \tag{2.9}$$

An adiabatic sidewall boundary condition (2.6) is relevant for experiments where tanks or cells are insulated at the sides, and will be implemented throughout the remainder of this paper. The Appendix gives the analytic result for the fixed-temperature sidewall boundary condition (2.5). The mixed (i.e. adiabatic) boundary condition case is more difficult to solve analytically, but solutions can still be written for the special case $Pr = 1$. This case will be described in detail in the following.

Trying solutions with an exponential growth time dependence ($e^{\lambda t}$), (2.9) simplifies and can be uncoupled by introducing two new fields $X(r, \theta)$ and $Y(r, \theta)$,

$$X(r, \theta) = w(r, \theta) - \Theta(r, \theta), \tag{2.10}$$

$$Y(r, \theta) = w(r, \theta) + \Theta(r, \theta), \tag{2.11}$$

that satisfy

$$\sqrt{Ra}(\lambda + 1)X = \frac{\partial^2 X}{\partial r^2} + \frac{1}{r}\frac{\partial X}{\partial r} + \frac{1}{r^2}\frac{\partial^2 X}{\partial \theta^2}, \tag{2.12}$$

$$\sqrt{Ra}(\lambda - 1)Y = \frac{\partial^2 Y}{\partial r^2} + \frac{1}{r}\frac{\partial Y}{\partial r} + \frac{1}{r^2}\frac{\partial^2 Y}{\partial \theta^2}. \tag{2.13}$$

The azimuthal dependence can be expanded as a combination of $\sin(n\theta)$ and $\cos(n\theta)$ and written in terms of the modes X_n and Y_n, which satisfy the modified Bessel equation:

$$r^2\frac{\mathrm{d}^2 X_n}{\mathrm{d}r^2} + r\frac{\mathrm{d}X_n}{\mathrm{d}r} - (\sqrt{Ra}(\lambda_{mn} + 1)\, r^2 + n^2)X_n = 0, \tag{2.14}$$

$$r^2\frac{\mathrm{d}^2 Y_n}{\mathrm{d}r^2} + r\frac{\mathrm{d}Y_n}{\mathrm{d}r} - (\sqrt{Ra}(\lambda_{mn} - 1)\, r^2 + n^2)Y_n = 0. \tag{2.15}$$

The m label for the growth rate is necessary because again there are multiple solutions for a given n, λ_{mn}, which satisfy the boundary conditions. The radial dependences of the solutions to (2.15) are

$$X_n(r) = x_0\, \mathrm{I}_n(\sqrt{(\lambda_{mn} + 1)}\, Ra^{1/4}\, r), \tag{2.16}$$

$$Y_n(r) = y_0\, \mathrm{I}_n(\sqrt{(\lambda_{mn} - 1)}\, Ra^{1/4}\, r), \tag{2.17}$$

where I_n is the modified Bessel function of the first kind. The modified Bessel functions of the second kind, K_n, are also solutions to (2.13) but are not physically acceptable because they diverge at $r = 0$.

The vertical velocity and temperature fields then have the form

$$w_n(r, t) = a_0\, \mathrm{e}^{\lambda_{mn} t}\, [Y_n(r) + X_n(r)], \tag{2.18}$$

$$\Theta_n(r, t) = a_0\, \mathrm{e}^{\lambda_{mn} t}\, [Y_n(r) - X_n(r)], \tag{2.19}$$

where the prefactor a_0 is unprescribed.

The growth rate of each mode λ_{mn} depends on Ra. After applying the boundary conditions at the cylinder wall at $r = r_{ext} = 1/2$ ((2.4) and (2.6)), the solutions

correspond to the roots of

$$-\sqrt{\frac{\lambda-1}{\lambda+1}}\,\frac{\mathrm{I}_n\left(\frac{1}{2}\sqrt{(\lambda+1)}\,Ra^{1/4}\right)}{\mathrm{I}_n\left(\frac{1}{2}\sqrt{(\lambda-1)}\,Ra^{1/4}\right)} = \frac{\mathrm{I}_{n-1}\left(\frac{1}{2}\sqrt{(\lambda+1)}\,Ra^{1/4}\right)+\mathrm{I}_{n+1}\left(\frac{1}{2}\sqrt{(\lambda+1)}\,Ra^{1/4}\right)}{\mathrm{I}_{n-1}\left(\frac{1}{2}\sqrt{(\lambda-1)}\,Ra^{1/4}\right)+\mathrm{I}_{n+1}\left(\frac{1}{2}\sqrt{(\lambda-1)}\,Ra^{1/4}\right)}. \tag{2.20}$$

Even though there are multiple solutions $\lambda = \lambda_{mn}$ for each mode n, the maximum growth rate – which always appears for the smallest m index – will dominate over the others as time progresses. In conclusion, while the n index is related to the number of oscillations (or nodes) of the solution along the azimuthal direction θ, the m mode is connected to the number of nodes along the radial direction r.

Intuitively one might guess that the exponential growth cannot be maintained, and would be arrested by friction on the sidewalls. However, the solutions to the above system of equations have not ignored viscous drag on the walls. Even though the velocity, and gradients at the walls, are growing exponentially, the frictional force does not overtake the driving buoyancy force.

In the periodic RB cell, the global, time-averaged dimensionless heat transfer is given as

$$Nu = \frac{\langle w\Theta\rangle}{\kappa\,\Delta'} + 1, \tag{2.21}$$

where the brackets indicate a volume (surface would be the same) and time average. When $|w| \sim \mathrm{e}^{\lambda_{mn}t}$ and $|\Theta| \sim \mathrm{e}^{\lambda_{mn}t}$, the instantaneous heat transfer $Nu(t) \sim \mathrm{e}^{2\lambda_{mn}t}$ also grows exponentially in time.

2.2.1. *Axisymmetric, dipolar modes and critical Rayleigh number*

The spatial form of solutions corresponding to the zero-mode case ($n = 0$) has an axisymmetric profile (see (2.17)). Obviously these zero-mode axisymmetric solutions have a non-zero mean vertical flow and non-zero mean temperature fluctuation, and so they are in conflict with the condition (2.7). Although these solutions are non-physical (they correspond to an unbounded infinite system), they will be useful in the following to validate our simulations.

From the above considerations we deduce that the first unstable physical mode is $n = 1$, which corresponds to a dipolar flow profile, moving upwards in half of the cylinder and downwards in the other half. Such dipolar modes were also observed in experiments in a cylindrical column (Cholemari & Arakeri 2009). The critical Rayleigh number corresponding to each mode can be computed from (2.20) by imposing $\lambda_{mn} = 0$, the value of n, and by looking at the mth zeros of the resulting equation:

$$-\mathrm{i}\,\frac{\mathrm{I}_n\left(\frac{1}{2}\,Ra^{1/4}\right)}{\mathrm{I}_n\left(\frac{\mathrm{i}}{2}\,Ra^{1/4}\right)} = \frac{\mathrm{I}_{n-1}\left(\frac{1}{2}\,Ra^{1/4}\right)+\mathrm{I}_{n+1}\left(\frac{1}{2}\,Ra^{1/4}\right)}{\mathrm{I}_{n-1}\left(\frac{\mathrm{i}}{2}\,Ra^{1/4}\right)+\mathrm{I}_{n+1}\left(\frac{\mathrm{i}}{2}\,Ra^{1/4}\right)}. \tag{2.22}$$

Ra	λ_{mn}	$m=1$	2	3
7.66×10^3	$n=0$	0.810	0.022	—
	1	0.520	—	—
	2	0.140	—	—
3.06×10^4	0	0.890	0.450	—
	1	0.730	0.120	—
	2	0.520	—	—
	3	0.260	—	—
1.23×10^5	0	0.940	0.700	0.2800
	1	0.860	0.520	0.0041
	2	0.740	0.310	—
	3	0.600	0.080	—
	4	0.440	—	—
	5	0.250	—	—
	6	0.040	—	—

TABLE 1. Positive growth rates λ_{mn} corresponding to active modes, for $Ra=7.66\times10^3$ (top), $Ra=3.06\times10^4$ (middle) and $Ra=1.23\times10^5$ (bottom) at $Pr=1$.

For the dipolar flow with $n=1, m=1$, we find $Ra_c=1087.397$. Note that the value of Ra_c coincides with the one derived by Batchelor & Nitsche (1993) once one has taken into account that these authors defined Ra based on the cylinder radius length rather than on the diameter, as in the present study.

In table 1 we list the active modes at different Ra numbers above Ra_c. For the specific case $Ra=7.66\times10^3$ and $Pr=1.0$, the $n=0$ maximum growth rate is $\lambda_{10}=0.81$. The first physical dipolar mode has growth rate $\lambda_{11}=0.52$. The growth rates and their spatial dependences are confirmed by our simulations and they will be discussed in the following sections.

3. Numerical method

Numerical simulations in a cylindrical cell are performed using the code developed by Verzicco & Orlandi (1996) and Verzicco & Camussi (2003), modified to satisfy the periodic conditions at $z=0, L$. Furthermore, to satisfy the condition (2.7), the vertical flow and mean temperature fluctuation are subtracted at each time step. A similar procedure was adopted in the earlier tri-periodic cell simulations by Lohse & Toschi (2003) and Calzavarini *et al.* (2005, 2006). A finite difference scheme on a staggered grid is used to directly solve the incompressible continuity, momentum equation and energy equations under the Boussinesq approximation using a fractional step method (Kim & Moin 1985; Verzicco & Orlandi 1996; Verzicco & Camussi 2003). The grid is non-uniform in the radial direction, but is uniform in z owing to the periodicity, allowing the pressure solver to take advantage of trigonometric expansions and making the routine more efficient. In the simulations we must fix the axial periodicity length L, which is here just a numerical parameter rather than a physical scale for the system dynamics. We expect, and will find, that, as the aspect ratio $\Gamma=d/L$ is reduced (by increasing the periodicity length L), the system properties become independent of Γ.

All the simulations have been started with a velocity field at rest and the temperature field consisting only of a random perturbation of maximum amplitude $0.01\Delta' d$.

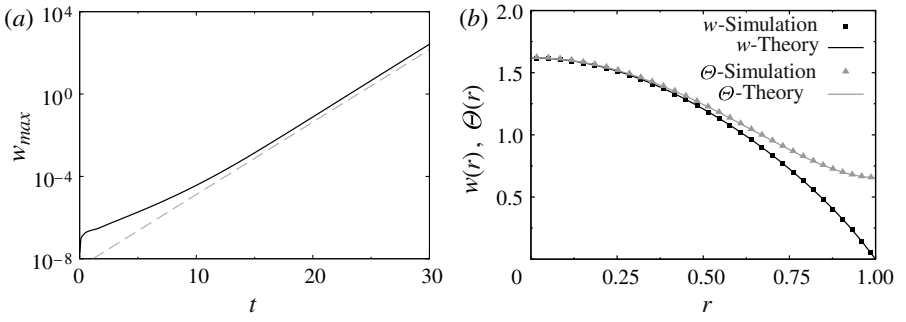

FIGURE 1. (*a*) Growth rate of vertical velocity field w for the $n = 0$ axisymmetric mode as a function of non-dimensional time; the simulation with $\Gamma = 1/2$ (solid black line) approaches the theoretical prediction of $\lambda_{10} = 0.81$ (dashed grey line). (*b*) Spatial forms of w and temperature fluctuation field Θ for $Ra = 7.66 \times 10^3$; the simulation and theory coincide.

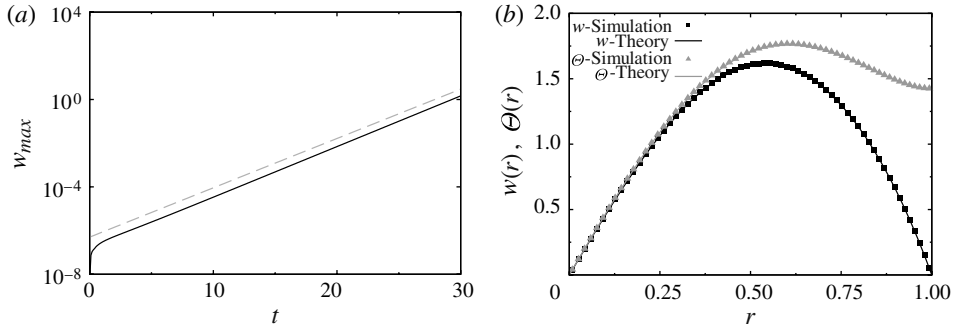

FIGURE 2. (*a*) Growth rate of vertical velocity field w for the $n = 1$ dipolar mode as a function of non-dimensional time; the simulation with $\Gamma = 1/2$ (solid black line) approaches the theoretical prediction of $\lambda_{10} = 0.52$ (dashed grey line). (*b*) Spatial forms of w and temperature fluctuation field Θ for $Ra = 7.66 \times 10^3$; the simulation and theory coincide.

The new code implementation with periodic conditions was first checked by direct comparison of the predicted growth rates and radial forms of w and Θ from the analysis in the previous section, both for cases where $n = 0$ and $n = 1$ modes dominated, along with the fixed-temperature sidewall boundary conditions (see Appendix). For $Ra = 7656$, $Pr = 1$ and $\Gamma = 1/2$, the axisymmetric and dipolar modes are isolated at early times and are shown in figures 1 and 2, comparing well with the theoretical predictions. Here, because the velocity and temperature fields are observed to be z-independent, we use the maximum vertical velocity field calculated at each time step to represent $a_0\, \mathrm{e}^{\lambda_{mn} t}$ from (2.19).

When only a few of the exponentially growing modes are active at low Ra (as for the parameters in table 1), the velocity and temperature gradients at $\theta_n = 2\pi/n$ grow exponentially and thus the resolution unavoidably becomes insufficient at some point. However, this is only an issue for low-Ra cells because, as more modes are available, their interaction prevents such a situation from occurring. We find that, though the resolution can affect the maximum w and Θ (and thus the heat transfer) obtained during the oscillations of the system, the growth rates are unaffected. For example, at $Ra = 7656$, $Pr = 1$ and $\Gamma = 1/4$ where the λ_{11} mode strongly dominates the system,

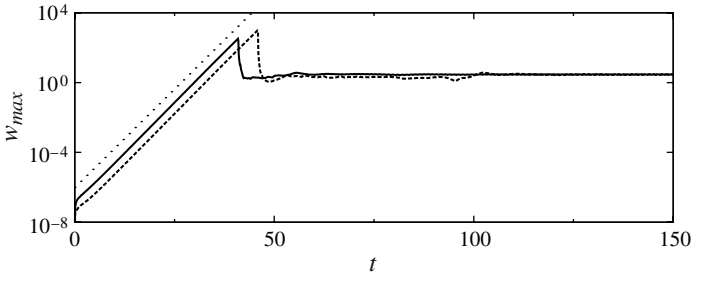

FIGURE 3. Exponential growth and stabilization of vertical velocity field w for $Ra = 7.66 \times 10^3$, $Pr = 1$ and $\Gamma = 1/4$ as a function of non-dimensional time, for resolutions $65 \times 33 \times 129$ (solid line) and $129 \times 65 \times 129$ (dashed line). The predicted growth rate of $\lambda_{11} = 0.52$ is shown as a dotted line.

Ra	Γ	$N_\theta \times N_r \times N_z$	Nu	Re	$\langle w^2 \rangle / \langle u_h^2 \rangle$	$\epsilon_u(\nabla_i u_j)/\epsilon_u(Nu)$	η/d
3.06×10^4	1/4	$129 \times 65 \times 257$	197	205	3.12	1.020	2.06×10^{-2}
1.23×10^5	1/2	$129 \times 65 \times 129$	384	428	2.50	0.970	1.29×10^{-2}
1.23×10^5	1/4	$129 \times 65 \times 257$	271	377	2.23	0.970	1.36×10^{-2}
4.90×10^5	1/2	$257 \times 129 \times 257$	678	880	—	1.000	7.95×10^{-3}
4.90×10^5	1/4	$257 \times 129 \times 513$	409	716	1.84	1.000	8.54×10^{-3}
4.90×10^5	1/8	$257 \times 129 \times 1025$	431	730	1.98	1.000	7.46×10^{-3}
7.84×10^6	1/2	$257 \times 129 \times 257$	4544	4702	2.49	0.832	2.79×10^{-3}
7.84×10^6	1/4	$257 \times 129 \times 513$	2349	3665	1.80	0.870	2.87×10^{-3}
7.84×10^6	1/8	$257 \times 129 \times 1025$	2196	3664	1.70	0.890	2.85×10^{-3}
1.57×10^7	1/4	$257 \times 129 \times 513$	2386	4747	1.59	0.830	2.4×10^{-3}
1.57×10^7	1/8	$257 \times 129 \times 1025$	3248	5349	1.76	0.820	2.2×10^{-3}
3.14×10^8	1/4	$257 \times 129 \times 1025$	12 191	22 909	1.43	0.550	8.5×10^{-4}

TABLE 2. Parameters and results from simulations. Columns contain Rayleigh number Ra, aspect ratio Γ, grid resolution (number of nodes in θ, r and z directions), Nusselt number Nu calculated by volume average of (2.21), Reynolds number Re calculated from mean fluctuating velocity, ratio of the vertical to horizontal energies in fluctuating fields, check of global relation of $\epsilon_u(\nabla_i u_j)$ calculated directly from velocity gradients compared to $\epsilon_u(Nu) \equiv (\nu^3\, Nu\, Ra\, Pr^{-2}\, d^{-4})$, and finally the non-dimensional Kolmogorov scale η calculated from the kinetic energy dissipation rate $\epsilon_u(\nabla_i u_j)$.

simulations with a resolution of $129 \times 65 \times 129$ (in θ, r, z) reach a maximum vertical velocity of $w_{max} = 1000$ before stabilizing, compared to $w_{max} = 200$ for a resolution of $65 \times 33 \times 129$ (shown in figure 3). Even though the early-time dynamics depends on the resolution, the growth rate and steady state that is reached are unaffected. The situation is analogous to what Calzavarini *et al.* (2006) found in the unconfined RB system.

The consistency of the code was also verified using the relation between the Nusselt number and the volume and time-averaged kinetic dissipation rate, $\epsilon_u = \nu |\nabla \boldsymbol{u}|^2$. For the periodic cell, $\epsilon_u = \nu^3\, Nu\, Ra\, Pr^{-2}\, d^{-4}$, which is confirmed within a few per cent as long as the spatial resolution of the simulation is adequate (see table 2). It should be noted that for increasing Ra the previous identity is verified less satisfactorily since

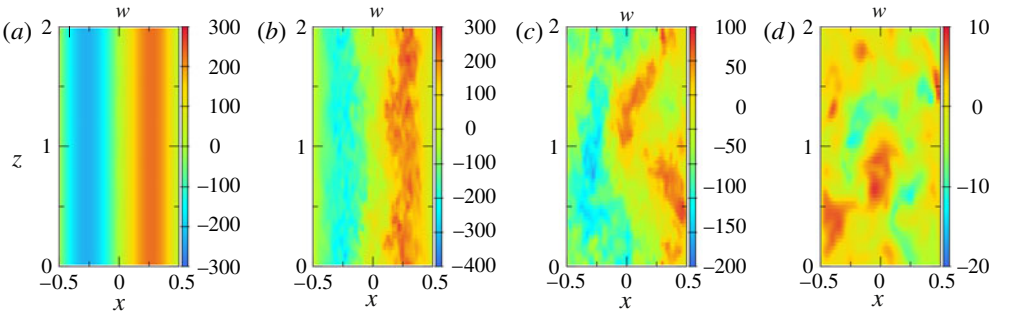

FIGURE 4. Instantaneous contour plots of the dimensionless vertical velocity w, through a vertical cross-section of the cell, for $Ra = 7.66 \times 10^3$, $Pr = 1$ and $\Gamma = 1/2$. Times are chosen as follows: just before stabilization of the growing dipolar mode at (*a*) $t = 99.9$; during stabilization when horizontal velocity fluctuations are growing at (*b*) $t = 99.96$ and (*c*)$t = 100.02$; and later after decay at (*d*) $t = 100.2$. Note that the colour/grey scales are varied according to the flow so that the structure can be seen at all times. A movie of the process is provided in the supplementary material available at http://dx.doi.org/10.1017/jfm.2011.440.

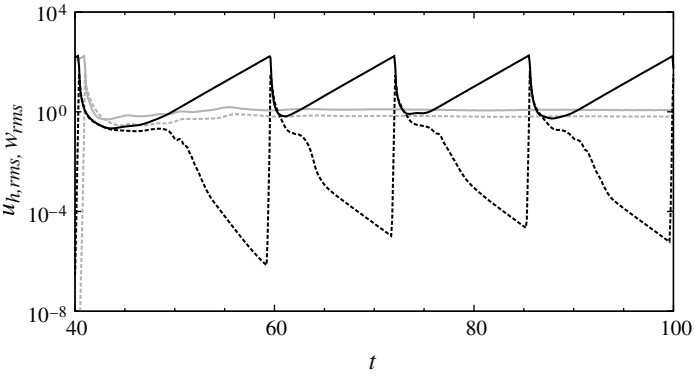

FIGURE 5. Aspect ratio dependence of mode growth and decay at $Ra = 7.66 \times 10^3$ and $Pr = 1$. Plotted are the r.m.s. vertical (solid line) and horizontal (u_h, dashed line) velocity components for $\Gamma = 1/2$ (black) and $\Gamma = 1/4$ (grey).

limitations of the computational resources prevented us from running cases on larger grids.

4. Results

At low Ra we observe individual growing modes which, depending on Ra and Γ, dominate the system dynamics. Already shown in figures 1–3 is the exponential growth at early times for simulations with $Ra = 7.66 \times 10^3$, $Pr = 1$ and $\Gamma = 1/2$ and $1/4$. After the initial growth at $\Gamma = 1/2$, figure 5 shows that the system temporarily stabilizes as horizontal velocity field fluctuations increase, which destroys the axially uniform modes of (2.9). This process continues periodically, with the horizontal field growing and decaying. This is visualized in figure 4, which shows snapshots of the dimensionless vertical velocity in a vertical cross-section through the axis of the cell, just before, during and after the stabilization process has occurred. Analogous

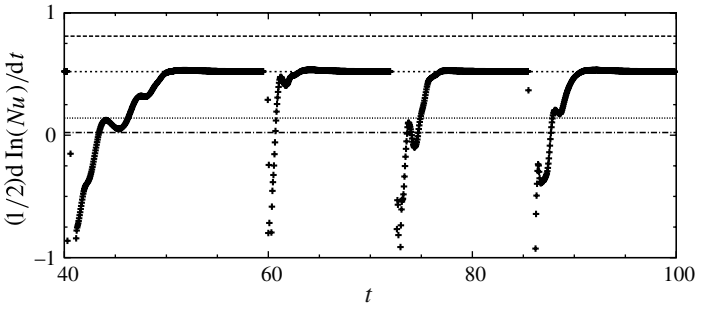

FIGURE 6. Plot of $(1/2)\,\mathrm{d}\ln(Nu)/\mathrm{d}t$, along with the active mode growth rates from table 1 for $Ra = 7.66 \times 10^3$ and $Pr = 1$, for $\Gamma = 1/2$. The axisymmetric mode with $\lambda_{10} = 0.81$ was suppressed, so the system periodically sets in on the next fastest growing mode $\lambda_{11} = 0.52$.

dynamics was observed in the tri-periodic homogeneous RB system of Calzavarini *et al.* (2006), and the process was found to depend sensitively on the numerical resolution and time step size. Here, we have an additional parameter, the periodicity length, which can affect this stabilization process. If the periodicity length is increased so that $\Gamma = 1/4$, instead of observing the long-term periodic behaviour, the system settles and stabilizes after the horizontal fluctuations become of the same order as the vertical fluctuations (figure 5). This indicates that the origin of the physical process that causes the destruction of the exponentially growing modes is related to the ability of the fluctuations to extend along the z direction.

Plotting $(1/2)\,\mathrm{d}\ln(Nu)/\mathrm{d}t$ as a function of time, along with the active λ_{mn}, clearly shows convergence of the system to the fastest growing mode for $Ra = 7.66 \times 10^3$ with $\Gamma = 1/2$ in figure 6.

As Ra is increased, more modes are present and the growth rates become closer together. This leads to interaction between the modes and stabilization of the system by preventing individual modes from dominating the flow. Figure 7 shows the time variation of the Nusselt number for $Ra = 1.23 \times 10^5$ for $\Gamma = 1/2$ and $\Gamma = 1/4$.

Though the observed maximum of growth rate jumps among the modes with lower growth rates, there is no prolonged exponential growth as was seen at lower Ra. There is again a difference between $\Gamma = 1/2$ and $1/4$ – the simulations at lower aspect ratio do not reach the same maximum growth rates, leading to a more stable system. For reference and comparison to figure 4 with $\Gamma = 1/2$, figure 8 shows a snapshot of the vertical velocity field in a $\Gamma = 1/8$ cell for $Ra = 7.85 \times 10^6$.

We have already seen that the aspect ratio of the cell, determined by the chosen numerical periodicity length, can affect the stabilization of the system by the breakdown of the exponentially growing modes (figures 5 and 7). Because we are interested in understanding the heat transfer and development of turbulence in a long pipe, when going to higher Ra one would hope that the results are unaffected by the choice of the periodicity length. Table 2 shows simulation results at $Ra = O(10^4$–$10^8)$ at aspect ratios $\Gamma = 1/8$, $1/4$ and $1/2$. The aspect ratio was changed by doubling the periodicity length, and keeping the resolution in z the same. It appears that the global system properties indeed start to converge once $\Gamma = 1/4$–$1/8$ for $Ra = O(10^5$–$10^6)$. For higher Ra, there is still aspect ratio dependence, but numerical limitations prevent us from increasing the periodicity length further. Since the $\Gamma = 1/4$ simulations require half the number of grid points with respect to longer cells with $\Gamma = 1/8$,

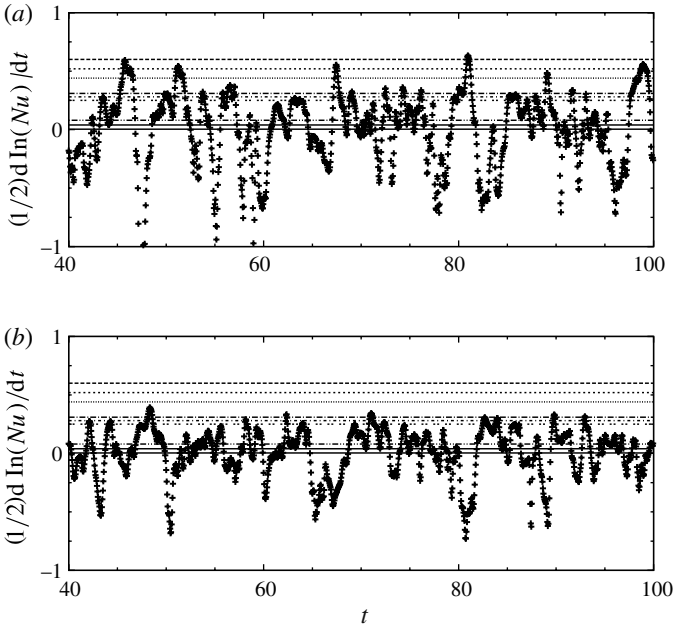

FIGURE 7. Plot of $(1/2)\,\mathrm{d}\ln(Nu)/\mathrm{d}t$ for $Ra = 1.23 \times 10^5$ and $Pr = 1$, for (*a*) $\Gamma = 1/2$ and (*b*) $\Gamma = 1/4$. The active mode growth rates reached by the system are shown by the horizontal lines at $\lambda = 0.60,\ 0.52,\ 0.44,\ 0.31,\ 0.28,\ 0.25,\ 0.080,\ 0.04,\ 0.0041$ from table 1.

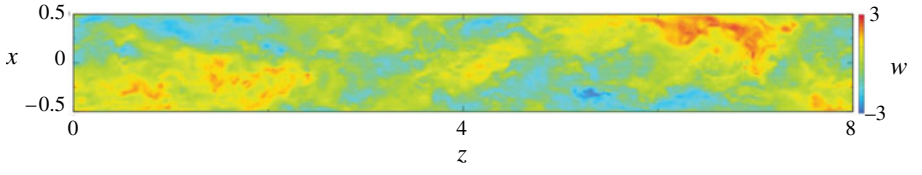

FIGURE 8. Instantaneous contour plot of the dimensionless vertical velocity w, through a vertical cross-section of the cell, for a typical state at $Ra = 7.84 \times 10^6$, $Pr = 1$ and $\Gamma = 1/8$.

higher-Ra simulations that already require a finer resolution are done with the intermediate aspect ratio $\Gamma = 1/4$.

The spatial variation of the root-mean-square (r.m.s.) velocity components plotted in figure 9 for various Ra shows the horizontal velocity $u_{h,rms}$ peaks at the axis, and goes to zero at the walls. The vertical velocity fluctuations peak closer to the walls, with a local minimum along the axis, falling to zero at the walls owing to friction. At lower Ra, the horizontal fluctuations do not reach the same size as the vertical fluctuations at the axis. As Ra is increased, $u_{h,rms}$ increases relative to w_{rms} at the axis, eventually overtaking w_{rms}. The horizontal fluctuations also become more uniform across the cell. The peaks in w_{rms} become sharper and move towards the outside.

Similar behaviour was observed in the measured profiles in the buoyancy-driven pipe turbulence experiments of Cholemari & Arakeri (2009). In their experiments with $Ra \approx 10^8$ and $Pr = 670$, the profiles resembled those of figure 9(*a*) for the lower $Ra = 3.06 \times 10^4$ and $Pr = 1$, but the horizontal fluctuations reached only about 60 % of the magnitude of the vertical fluctuations at the axis. The reason for the resemblance

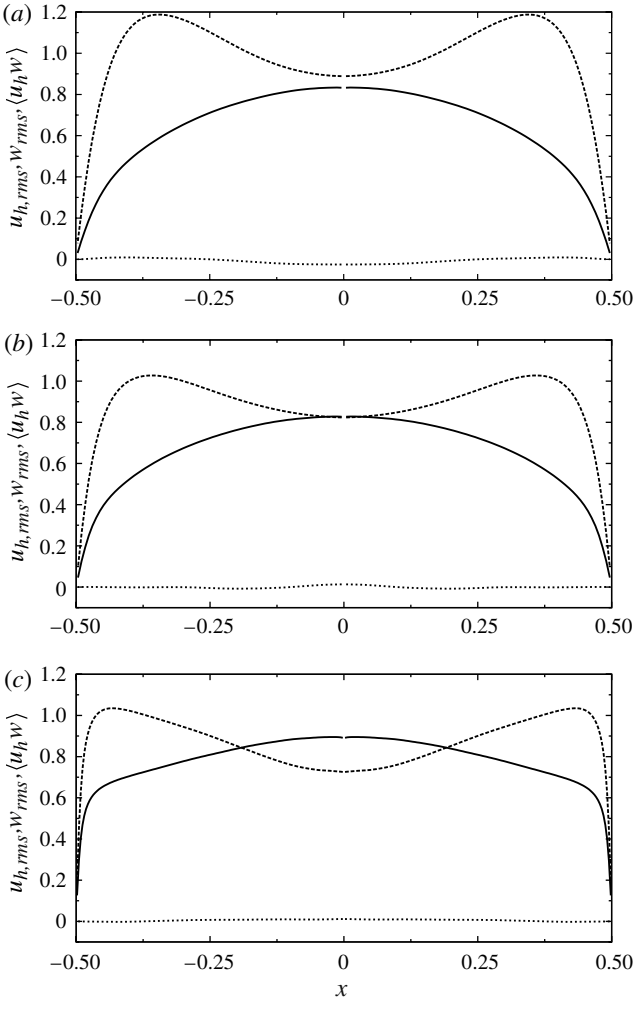

FIGURE 9. Spatial variations of r.m.s. horizontal ($u_{h,rms}$, solid line) and vertical (w_{rms}, dashed line) velocities, and of the turbulent shear stress ($\langle u_h w \rangle$, dotted line) for $\Gamma = 1/4$ and $Pr = 1$ at (*a*) $Ra = 3.06 \times 10^4$, (*b*) $Ra = 1.23 \times 10^5$ and (*c*) $Ra = 1.57 \times 10^7$.

to the lower-Ra result here is almost certainly the high value of Pr. To check, we also calculated that the turbulent shear stress $\langle u_h w \rangle$ was absent across the cell. For all cases, $\langle u_h w \rangle$ is close to zero compared to the r.m.s. components. As in the experiments, the system remains anisotropic, evidenced by the fact that $\langle w^2 \rangle / \langle u_h^2 \rangle \neq 1/2$, especially near the walls, where the horizontal fluctuations fall to zero much more rapidly than the vertical fluctuations.

Counter-intuitively, the heat transfer at low $Ra = O(10^4)$ and smaller is very large owing to single exponential modes dominating the system in this regime. For these systems, it is inappropriate to define an average Nu or Re because we have seen that the maximum peaks (as in figure 5) depend on the grid resolution. As Ra is increased, the system stabilizes as a result of mode interaction and the scaling appears consistent with $Nu \sim Ra^{1/2}$ for $Ra = O(10^5$–$10^8)$, as shown in figure 10. The values used to determine the scaling law come from the runs at aspect ratio 1/4 (given in

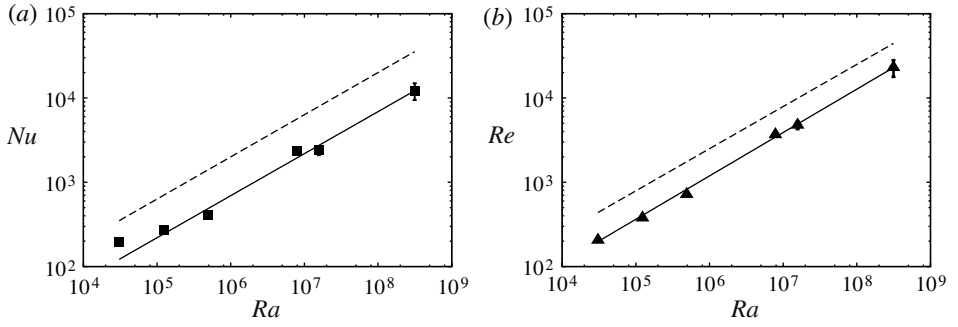

FIGURE 10. Scaling of (*a*) Nusselt number *Nu* and (*b*) Reynolds number *Re* with *Ra* for $\Gamma = 1/4$ data. Dashed lines have slope 1/2 for comparison. The power-law fits (solid lines) have slopes of 0.50 ± 0.06 for *Nu* and 0.51 ± 0.05 for *Re*.

table 2). Errors are estimated by the percentage difference between the two methods to calculate the Nusselt number (one being the volume average in (2.21), the other being via the global relation with the kinetic energy dissipation rate). The highest *Ra* runs appear under-resolved but nevertheless the prediction confirms the scaling laws. The mean Reynolds number is calculated as $Re = \langle u^2 \rangle_{V,t}^{1/2} d/\nu$ (where u is the total dimensional velocity), and also appears consistent with the 1/2 power law from figure 10. In Cholemari & Arakeri (2005) a mixing length model for the amplitude of *Nu* and $Re_z \equiv \langle w^2 \rangle_{V,t}^{1/2} d/\nu$ versus *Ra* and *Pr* was proposed. This model uses as input the fits to the experimental data (at $Pr = 670$) and is therefore able to provide not only the scaling exponents but also the prefactors. Cholemari & Arakeri (2005) provide, in the limit of $\Gamma \to \infty$, the following scaling laws: $Nu = C_m Ra^{1/2} Pr^{1/2}$ and $Re_z = K Ra^{1/2} Pr^{-1/2}$ with $C_m = 0.88$ and $K \simeq 1$. The power-law fit, $a Ra^b$, to our numerical results (all at $Pr = 1$) gives here $C_m = 0.7 \pm 0.3$ and $K = 0.9 \pm 0.1$, in close agreement with the mixing length model.

5. Conclusions

We have presented theoretical results and simulations of thermal convection in a laterally confined cylindrical pipe in the limit of small aspect ratios. At low *Ra* we find exponentially growing modes consisting of upward- and downward-flowing columns, analogous to those found in homogeneous RBC with no boundaries and simulations in tri-periodic cells (Calzavarini *et al.* 2005, 2006), along with experimental observations (Gibert *et al.* 2006, 2009; Cholemari & Arakeri 2009). The breakdown of these modes is found to depend on the numerical aspect ratio of the cell (or periodicity length), implying that their destruction is related to the ability of disturbances in the cross-axial direction to grow. At higher *Ra*, the scaling of the heat transfer and turbulence are consistent with the predicted (Grossmann & Lohse 2000, 2001, 2002) $Nu \sim \sqrt{Ra}$ and $Re \sim \sqrt{Ra}$ scaling of the ultimate, bulk-dominated regime of thermal convection, just as in the case of the tri-periodic boundary conditions (Lohse & Toschi 2003; Calzavarini *et al.* 2005). Furthermore, the measured amplitudes for *Nu* and *Re* are in agreement with the mixing length model by Cholemari & Arakeri (2005).

It is remarkable that the sidewall boundary conditions and the resulting kinematic boundary layers do *not* lead to different scaling behaviours with a less steep increase of *Nu* with *Ra*, as common for the lower-*Ra* regimes, say $Ra \leqslant 10^{12}$,

in the unifying theory of Grossmann & Lohse (2000, 2001, 2002). The reason must be that these kinetic boundary layers only form at the sidewalls, and not at the top and bottom walls, which do not exist in our setup. We therefore do not expect a less steep increase of Nu with Ra beyond the onset of turbulence in the lateral kinetic boundary layers, which is expected to occur beyond a critical shear Reynolds number $Re_s^* \approx 0.5\sqrt{Re} \approx 420$ (Landau & Lifshitz 1987; Grossmann & Lohse 2000, 2002, 2011). We note that here we are still considerably below this transition, as even for our largest Ra we only have $Re_s \approx 75 \ll Re_s^*$. It would be worth while to push the numerical simulations in this laterally confined geometry to Ra numbers beyond the onset of the shear instability, in order to confirm that also then $Nu \sim Re \sim Ra^{1/2}$, without any logarithmic corrections, which seem to be typical for ultimate RB flow (and analogous ultimate Taylor–Couette flow) in *fully confined* (i.e. with boundaries and boundary layers also towards the top and bottom) geometries (Chavanne *et al.* 1997, 2001; Dubrulle 2001; van Gils *et al.* 2011; Grossmann & Lohse 2011).

Acknowledgements

The authors acknowledge the National Computing Facilities (NCF) for awarding us computing time on SARA in Amsterdam. We thank V. Lavezzo for careful reading of the manuscript. We also thank the EU COST Action MP0806. Finally, we acknowledge the anonymous referee (no. 4) for drawing our attention on the important work by Batchelor & Nitsche on the same subject.

A supplementary movie is available at http://dx.doi.org/10.1017/jfm.2011.440.

Appendix. Zero temperature fluctuations at sidewall solution

Though this boundary condition is not currently relevant for the experiments, it has a simple solution, which was used to check the numerical results. Zero temperature fluctuations at the sidewall means that physically the absolute temperature follows the imposed linear profile at the walls. Equation (2.9) is exactly satisfied by solutions of the form

$$w_{mn}(r,\theta,t) = w_0\, \mathrm{e}^{\lambda_{mn} t} \cos(n\theta)\, \mathrm{J}_n(k_{mn} r), \tag{A 1}$$

$$\Theta_{mn}(r,\theta,t) = \Theta_0\, \mathrm{e}^{\lambda_{mn} t} \cos(n\theta)\, \mathrm{J}_n(k_{mn} r), \tag{A 2}$$

where J_n is the nth Bessel function of the first kind ($\sin(n\theta)$ dependence is also acceptable). The growth rates λ_{mn} and wavenumbers k_{mn} are determined via the boundary conditions (2.4) and (2.5). Here with $w(r=1/2) = \Theta(r=1/2) = 0$, $k_{m,n}$ is related to the ρ_{mn} (the m th root of J_n) by

$$k_{mn} = \frac{\rho_{mn}}{r_{ext}} = \frac{\rho_{mn}}{1/2}. \tag{A 3}$$

The dispersion relation determining the growth rate for each mode is given by

$$2\sqrt{Pr\,Ra}\,\lambda_{mn} = -{k_{mn}}^2\,(1+Pr) + \sqrt{{k_{mn}}^4(1+Pr)^2 + 4\,Pr\,\left(Ra - {k_{mn}}^4\right)}, \tag{A 4}$$

which has the same form as the tri-periodic case (up to a constant factor, owing to the different choices for non-dimensionalization), but the allowed values of k_{mn} differ because of the geometry. Relation (A 4) is valid for any Pr value. The critical Rayleigh number for the $Pr = 1$ case, i.e. for $\lambda_{1,1}(Ra_c, Pr = 1) = 0$, is $Ra_c = {k_{11}}^4 = 3448.964$.

REFERENCES

AHLERS, G., GROSSMANN, S. & LOHSE, D. 2009 Heat transfer and large scale dynamics in turbulent Rayleigh–Bénard convection. *Rev. Mod. Phys.* **81**, 503.

ARAKERI, J. H., AVILA, F. E., DADA, J. M. & TOVAR, R. O. 2000 Convection in a long vertical tube due to unstable stratification – a new type of turbulent flow? *Curr. Sci.* **79** (6), 859–866.

BATCHELOR, G. K. & NITSCHE, J. M. 1991 Instability of stationary unbounded stratified fluid. *J. Fluid Mech.* **227**, 357–391.

BATCHELOR, G. K. & NITSCHE, J. M. 1993 Instability of stratified fluid in a vertical cylinder. *J. Fluid Mech.* **252**, 419–448.

BIFERALE, L., CALZAVARINI, E., TOSCHI, F. & TRIPICCIONE, R. 2003 Universality of anisotropic fluctuations from numerical simulations of turbulent flows. *Europhys. Lett.* **64** (4), 461–467.

CALZAVARINI, E., DOERING, C. R., GIBBON, J. D., LOHSE, D., TANABE, A. & TOSCHI, F. 2006 Exponentially growing solutions of homogeneous Rayleigh–Bénard flow. *Phys. Rev.* E **73**, R035301.

CALZAVARINI, E., LOHSE, D., TOSCHI, F. & TRIPICCIONE, R. 2005 Rayleigh and Prandtl number scaling in the bulk of Rayleigh–Bénard turbulence. *Phys. Fluids* **17**, 055107.

CELANI, A., MAZZINO, A., SEMINARA, A. & TIZZI, M. 2007 Droplet condensation in two-dimensional Bolgiano turbulence. *J. Turbul.* **8**, 1–9.

CHAVANNE, X., CHILLA, F., CASTAING, B., HEBRAL, B., CHABAUD, B. & CHAUSSY, J. 1997 Observation of the ultimate regime in Rayleigh–Bénard convection. *Phys. Rev. Lett.* **79**, 3648–3651.

CHAVANNE, X., CHILLA, F., CHABAUD, B., CASTAING, B. & HEBRAL, B. 2001 Turbulent Rayleigh–Bénard convection in gaseous and liquid He. *Phys. Fluids* **13**, 1300–1320.

CHOLEMARI, M. & ARAKERI, J. 2005 Experiments and a model of turbulent exchange flow in a vertical pipe. *Intl J. Heat Mass Transfer* **48** (21–22), 4467–4473.

CHOLEMARI, M. & ARAKERI, J. 2009 Axially homogeneous, zero mean flow buoyancy-driven turbulence in a vertical pipe. *J. Fluid Mech.* **621**, 69–102.

DUBRULLE, B. 2001 Momentum transport and torque scaling in Taylor–Couette flow from an analogy with turbulent convection. *Eur. Phys. J.* B **21**, 295.

GARAUD, P., OGILVIE, G., MILLER, N. & STELLMACH, S. 2010 A model of the entropy flux and Reynolds stress in turbulent convection. *Mon. Not. R. Astron. Soc.* **407**, 2451–2467.

GIBERT, M., PABIOU, H., CHILLA, F. & CASTAING, B. 2006 High-Rayleigh-number convection in a vertical channel. *Phys. Rev. Lett.* **96**, 084501.

GIBERT, M., PABIOU, H., TISSERAND, J.-C., GERTJERENKEN, B., CASTAING, B. & CHILLÀ, F. 2009 Heat convection in a vertical channel: plumes versus turbulence diffusion. *Phys. Fluids* **21**, 035109.

VAN GILS, D., HUISMAN, S. G., BRUGGERT, G. W., SUN, C. & LOHSE, D. 2011 Torque scaling in turbulent Taylor–Couette flow with co- and counter-rotating cylinders. *Phys. Rev. Lett.* **106**, 024502.

GROSSMANN, S. & LOHSE, D. 2000 Scaling in thermal convection: a unifying theory. *J. Fluid Mech.* **407**, 27–56.

GROSSMANN, S. & LOHSE, D. 2001 Thermal convection for large Prandtl number. *Phys. Rev. Lett.* **86**, 3316–3319.

GROSSMANN, S. & LOHSE, D. 2002 Prandtl and Rayleigh number dependence of the Reynolds number in turbulent thermal convection. *Phys. Rev.* E **66**, 016305.

GROSSMANN, S. & LOHSE, D. 2011 Multiple scaling in the ultimate regime of thermal convection. *Phys. Fluids* **23**, 045108.

HALESA, L. 1937 Convection currents in geysers. *Mon. Not. R. Astron. Soc. Geophys. Suppl.* **4**, 122.

JONES, C. A. & MOORE, D. R. 1979 The stability of axisymmetric convection. *Geophys. Astrophys. Fluid Dyn.* **11**, 245–270.

KADANOFF, L. P. 2001 Turbulent heat flow: structures and scaling. *Phys. Today* **54** (8), 34–39.

KIM, J. & MOIN, P. 1985 Application of a fractional-step method to incompressible Navier–Stokes equations. *J. Comput. Phys.* **59**, 308–323.

KRAICHNAN, R. H. 1962 Turbulent thermal convection at arbitrary Prandtl number. *Phys. Fluids* **5**, 1374–1389.

LANDAU, L. D. & LIFSHITZ, E. M. 1987 *Fluid Mechanics*. Pergamon.

LOHSE, D. & TOSCHI, F. 2003 The ultimate state of thermal convection. *Phys. Rev. Lett.* **90**, 034502.

LOHSE, D. & XIA, K.-Q. 2010 Small-scale properties of turbulent Rayleigh–Bénard convection. *Annu. Rev. Fluid Mech.* **42**, 335–364.

PERRIER, F., MORAT, P. & LEMOUEL, J. L. 2002 Dynamics of air avalanches in the access pit of an underground quarry. *Phys. Rev. Lett.* **89**, 134501.

SIGGIA, E. D. 1994 High Rayleigh number convection. *Annu. Rev. Fluid Mech.* **26**, 137–168.

SIMITEV, R. D. & BUSSE, F. H. 2010 Problems of astrophysical turbulent convection: thermal convection in a layer without boundaries. In *Center for Turbulence Research, Proceedings of the Summer Program, 2010, Stanford University, CA* (ed. Parviz Moin, Johan Larsson & Nagi Mansour), website where the proccedings can be found: http://www.stanford.edu/group/ctr/Summer/SP10/.

SPIEGEL, E. A. 1971 Convection in stars. *Annu. Rev. Astron. Astrophys.* **9**, 323–352.

TAYLOR, G. I. 1954 Diffusion and mass transport in tubes. *Proc. Phys. Soc.* B **67**, 857–869.

TISSERAND, J.-C., CREYSSELS, M., GIBERT, M., CASTAING, D. & CHILLÀ, F. 2010 Convection in a vertical channel. *New J. Phys.* **12**, 075024.

VERZICCO, R. & CAMUSSI, R. 2003 Numerical experiments on strongly turbulent thermal convection in a slender cylindrical cell. *J. Fluid Mech.* **477**, 19–49.

VERZICCO, R. & ORLANDI, P. 1996 A finite-difference scheme for three-dimensional incompressible flow in cylindrical coordinates. *J. Comput. Phys.* **123**, 402–413.